



PCCP

Mechanical, Thermal, and Electrochemical Properties of Pr Doped Ceria from Wafer Curvature Measurements

Journal:	<i>Physical Chemistry Chemical Physics</i>
Manuscript ID	CP-ART-07-2018-004802.R2
Article Type:	Paper
Date Submitted by the Author:	16-Oct-2018
Complete List of Authors:	Ma, Yuxi; Michigan State University, Chemical Engineering and Materials Science Department Nicholas, Jason; Michigan State University, Chemical Engineering and Materials Science Department

SCHOLARONE™
Manuscripts



Journal Name

ARTICLE

Mechanical, Thermal, and Electrochemical Properties of Pr Doped Ceria from Wafer Curvature Measurements

Yuxi Ma^a and Jason D. Nicholas^{*a}Received 00th January 20xx,
Accepted 00th January 20xx

DOI: 10.1039/x0xx00000x

www.rsc.org/

This work demonstrates, for the first time, that a variety of disparate and technologically-relevant thermal, mechanical, and electrochemical oxygen-exchange material properties can all be obtained from *in situ*, current-collector-free wafer curvature measurements. Specifically, temperature or oxygen partial pressure induced changes in the curvature of 230 nm thick (100)-oriented Pr_{0.1}Ce_{0.9}O_{1.95-x} (10PCO) films atop 200 μm thick single crystal yttria stabilized zirconia or magnesium oxide substrates were used to measure the biaxial modulus, Young's Modulus, thermal expansion coefficient, thermo-chemical expansion coefficient, oxygen nonstoichiometry, chemical oxygen surface exchange coefficient, oxygen surface exchange resistance, thermal stress, chemical stress, thermal strain, and chemical strain of the model mixed ionic electronic conducting material 10PCO. The (100)-oriented thin film 10PCO thermal expansion coefficient, thermo-chemical expansion coefficient, oxygen nonstoichiometry and Young's Modulus (which is essentially constant, at ~200 MPa, over the entire 280-700°C temperature range in air) measured here were similar to those from other bulk and thin film 10PCO studies. In addition, the measured PCO10 oxygen surface coefficients were in agreement with those reported by other *in situ*, current-collector-free techniques. Taken together, this work highlights the advantages of using a sample's mechanical response, instead of the more traditional electrical response, to probe the electrochemical properties of the ion-exchange materials used in solid oxide fuel cell, solid oxide electrolysis cell, gas-sensing, battery, emission control, water splitting, water purification, and other electrochemically-active devices.

1. Introduction

A variety of materials, including those used in batteries,^{1, 2} fuel cells,³⁻⁷ electrolysis cells,⁸⁻¹¹ oxide memristors,^{12, 13} electrostrictive actuators,^{14, 15} gas separation units,¹⁶ chemical sensors,¹⁷ electrochromic windows,¹⁸ catalytic converters,¹⁹ etc., obtain their functionality from a high concentration of ionic point defects. Since point defect concentration changes typically result in lattice parameter changes,^{6, 20, 21} a coupling exists between the mechanical and electrochemical states of most high performance mixed ionic electronic conducting (MIEC) materials.²² In traditional (i.e. non thin film) batteries, solid oxide fuel cells (SOFCs), solid oxide electrolysis cells (SOECs) and other electrochemical devices utilizing bulk (i.e. >> 100 nm) particles, this mechano-chemical coupling is problematic because it produces stress gradients that crack and mechanically pulverize

the material when these MIEC material experience compositional changes during device operation.²³⁻²⁵ However, the higher fracture toughness's and higher Griffiths critical cracking stresses exhibited by thin film materials²⁶ have spurred interest in using externally applied stress to intentionally increase the point defect concentrations and electrochemical performance of thin film MIEC devices.²⁷⁻³³

For either situation, knowledge of a material's *in situ* / *in operando* mechanical, thermal and electrochemical properties is critical for engineering the stress profiles that help determine device performance and durability. Unfortunately, such data is scarce in the existing literature, especially at the elevated temperatures often encountered during device operation. Further, significant variation exists in the measured values, as evidenced by the 2, 3, and 4 order of magnitude differences in the 650°C chemical oxygen surface exchange coefficients of the common SOFC materials Ce_{0.9}Gd_{0.1}O_{1.95-δ},³⁴ La_{0.6}Sr_{0.4}Fe_{0.8}Co_{0.2}O_{3-δ},^{35, 36} and La_{0.6}Sr_{0.4}FeO_{3-δ}.³⁷⁻⁴⁰ Complicating matters, individual techniques capable of performing *in situ* or *in operando* measurements on such a disparate set of material properties (i.e. the mechanical, thermal, and electrochemical properties) have been absent from the literature.

The present work demonstrates for the first time that the biaxial modulus (M), Young's Modulus (E), thermal expansion

Department of Chemical Engineering and Materials Science, Michigan State University,
428 S. Shaw Lane, Room 2100, East Lansing, MI 48824, USA
*Email: jdn@msu.edu

† Footnotes relating to the title and/or authors should appear here.
Electronic Supplementary Information (ESI) available: [details of any supplementary information available should be included here]. See DOI: 10.1039/x0xx00000x

coefficient (α_t), thermo-chemical expansion coefficient (α_{tc}), oxygen nonstoichiometry (δ), chemical oxygen surface exchange coefficient (k), and oxygen surface exchange resistance (R_S) of a single material (in this case $\text{Pr}_{0.1}\text{Ce}_{0.9}\text{O}_{1.95}$ (10PCO)) can all be obtained as a function of simultaneously measured total stress (σ_{Total}), thermal stress (σ_t), chemical stress (σ_c), total strain (ε_{Total}), thermal strain (ε_c), chemical strain (ε_t), temperature (T), and oxygen partial pressure (p_{O_2}) conditions using *in situ*, non-contact, current-collector-free wafer curvature measurements. Doped ceria was chosen for this study due to its importance as a catalytic converter oxidation catalyst,^{19, 41} oxygen sensor material,⁴² water-splitting/alternative fuel production catalyst,^{11, 43} and SOFC/SOEC material.⁴⁴⁻⁴⁶ 10PCO in particular was chosen because of its conveniently large chemical expansion coefficient,⁴⁷ easily accessible mechano-chemically active state (it is mechano-chemically active in air above $\sim 380^\circ\text{C}$),⁴⁸ well-established point defect model,⁴⁹ and status as a model material.⁴⁹

2. Mechanics Theory

2.1 Wafer Curvature to Measure In Situ Film Stress

Mechanics theory indicates that the biaxial stress (σ_{Total}) within a dense thin film atop a dense thick substrate (such that the film thickness (h_f) to substrate thickness (h_s) ratio is less than 0.001) can be extracted from the wafer curvature (κ) (without knowledge of the film elastic properties) using Stoney's Equation:

$$\sigma_{Total} = \kappa \frac{M_S h_s^2}{6h_f} \quad [1]$$

where M_S is the substrate biaxial modulus defined as

$$M_S = \frac{E_s}{(1-\nu_s)} \quad [2]$$

where E_s is the substrate Young's modulus, and ν_s is the substrate Poisson's Ratio.⁵⁰⁻⁵² Hence, Equation 1 was used to extract the *in situ* film stress from the wafer curvature using the procedures described in the Experimental Methods of Section 3.

2.2 Dual Substrate Stress-Temperature Measurements to Determine Film Elastic and Expansion Coefficients

Previous studies have shown that the stress-temperature behaviour of electrochemically inactive thin films atop multiple substrates can be used to determine thin film elastic constants and thermal expansion coefficients.⁵³⁻⁵⁵ Here, this approach was extended, for the first time, to also measure the thin film thermo-chemical expansion coefficients of mechano-chemically active materials. Specifically, the stress-temperature derivatives ($\frac{\partial\sigma}{\partial T}$) of 10PCO thin films atop two mechano-chemically inactive substrates with different thermal expansion coefficients (i.e. $(\text{Y}_2\text{O}_3)_{0.095}(\text{ZrO}_2)_{0.905}$ (YSZ) and MgO with average 280-700°C thermal expansion coefficient (α_t) values of 9.5 and 14.3 ppm/°C, respectively) were measured and related to the film biaxial modulus (M_f), the substrate thermal expansion coefficients (α_1 and α_2), and the film thermo-chemical expansion coefficient (α_{tc}) using the relationships:

$$\frac{\partial\sigma_1}{\partial T} = M_f(\alpha_1 - \alpha_{tc}) \quad [3]$$

and

$$\frac{\partial\sigma_2}{\partial T} = M_f(\alpha_2 - \alpha_{tc}) \quad [4]$$

Application of temperature-dependent substrate thermal expansion data calculated from the literature^{56, 57} (shown in Figure S1 of the Supplemental Materials) to Equations 3 and 4, allowed M_f and α_{tc} to be determined by solving these two equations (both with two unknowns) simultaneously. For those temperatures where mechano-chemical coupling was inactive as indicated by previous 10PCO oxygen nonstoichiometry measurements (i.e. below $\sim 380^\circ\text{C}$),^{48, 49, 58-61} the thermo-chemical expansion coefficient was treated as simply representing the thermal expansion coefficient.

The film Young's modulus (E_f) was then determined from the measured M_f data using the definition of the biaxial modulus (shown in Equation 2) by assuming a 10PCO film Poisson's ratio (ν_f) of 0.33 (a common value for isotropic solids), as has been done previously in the literature for 10PCO.^{62, 63} (Note, ν_f could also have been measured directly by performing experiments on anisotropic substrates, as has been done in the literature,⁶⁴ but this was not attempted here based, in part, on the minor temperature variation in Poisson's Ratio observed for most materials, even as they encounter oxygen nonstoichiometries greater than those encountered here^{65, 66}).

2.3 Extraction of the Film Strains, Oxygen Nonstoichiometry, and Film Stresses from Dual Substrate Stress-Temperature Measurements

The total film strain (ε_{Total}) was extracted from the measured film stress (σ_{Total}) by assuming the film and substrate behaved as elastic solids and applying the thin film version of Hooke's Law:⁵¹

$$\varepsilon_{Total} = \sigma_{Total}/M \quad [5]$$

The ceria, YSZ, and MgO in this study were elastic over the entire 280-700°C temperature range evaluated here as demonstrated by the reproducible stress-curvature trajectories in in Figure S2 of the Supplemental Materials. This is consistent with the disappearance of ceria's oxygen-vacancy-induced elastic dipole anelasticity¹⁵ above $\sim 250^\circ\text{C}$.⁶⁷

Since literature studies have shown that 10PCO exhibits essentially no oxygen nonstoichiometry below 380°C,^{48, 49, 58-61} and⁶⁰

$$\varepsilon_{Total} = \varepsilon_t + \varepsilon_c \quad [6]$$

the 280-380°C chemical strain (ε_c) was assumed to be zero such that the 280-380°C ε_{Total} represented only the thermal strain (ε_t). A similar argument was made for the 280-380°C chemical, thermal, and total stress. As a rough approximation, the 280-380°C ε_t was assumed to vary linearly with temperature, in keeping with previous reports of the near-linear thermal expansion of 10PCO,^{58, 68} doped ceria,^{69, 70} 8YSZ⁶⁹ and MgO⁷¹ over the 280-700°C temperature range. As shown in Figure S3 of the Supplemental Materials, ε_t was then extrapolated to

temperatures > 380°C using this linear fit so that ε_c could be extracted from ε_{Total} via Equation 6. A similar treatment was given to the 380-700°C thermal and chemical stress data.

With knowledge of ε_c , the thin film 10PCO oxygen nonstoichiometry (δ) was determined using the relationship:^{20, 60, 72}

$$\varepsilon_c = \frac{\Delta l}{l} \Big|_T = \alpha_c \Delta \delta \quad [7]$$

using a (100) oriented 10PCO chemical expansion coefficient (α_c) of 0.067¹⁵ and a $\delta = 0$ below 380°C (as has been assumed in other studies^{60, 61}). Use of a constant α_c was warranted over the 280-700°C range because of the dilute nature of the oxygen vacancies encountered here ($\delta < 0.016$) and the fact that past ceria experimental^{60, 73-77} and modelling^{15, 20, 78} studies have shown that the lattice strain per oxygen vacancy (i.e. α_c) is constant for $\delta < 0.03$ and temperatures up to 1000°C (in particular, past studies on 10PCO have shown that α_c remains constant to at least $\delta = 0.055$).^{58, 60} A α_c value of 0.067 was chosen because that is the DFT-predicted value for (100) oriented ceria¹⁵ and is consistent with the 650-800°C 10PCO $\alpha_c = 0.064 \pm 0.005$ measured previously on YSZ supported (100) oriented 10PCO thin films⁷⁷ (although convenient, a constant α_c is not required to reliably extract materials properties from wafer curvature measurements).

2.4 Wafer Curvature Relaxation Measurements to Determine Oxygen Surface Exchange Behaviour

500-600°C chemical oxygen surface exchange coefficient (k) measurements were performed by fitting the wafer curvature response to a small, sudden change in p_{O_2} with the solution to Fick's Second Law for oxygen transfer into a surface controlled membrane:⁷⁹

$$\frac{\kappa - \kappa_0}{\kappa_\infty - \kappa_0} = \frac{\delta - \delta_0}{\delta_\infty - \delta_0} = 1 - \exp\left(-\frac{kt}{h_f}\right) \quad [8]$$

where κ is the wafer curvature at time (t), a 0 subscript denotes an initial value, an ∞ subscript denotes a new- p_{O_2} equilibrated value, and the other variables have their previously defined meanings. This solution to Fick's Second Law was justified because the 230 nm thick films examined here were >1000 times thinner than the 500-600°C 10PCO characteristic thickness,

$$L_c = D/k \quad [9]$$

(where D is the chemical diffusivity for oxygen) reported previously in the literature.⁴⁵

With knowledge of k and δ in air and ten times diluted air, the oxygen surface exchange resistance (R_S) (which is the area specific resistance for oxygen exchange into a dense material used in many SOFC electrode performance modelling studies^{80, 81}) was determined using the relation:^{45, 82}

$$R_S = \frac{RT}{4F^2 c_o k_q} \quad [10]$$

where R is the ideal gas constant, T is the absolute temperature, F is Faraday's constant, c_o is the lattice oxygen concentration, and

k_q is the electrical oxygen surface exchange coefficient. c_o was calculated from δ using the expression:

$$c_o = \frac{4(2 - \delta)}{a^3 * N_A} \quad [11]$$

where N_A is Avogadro's Number and a is the 10PCO lattice constant at temperature T reported in the literature.⁵⁸ k_q was calculated from the chemical oxygen surface exchange coefficient, k , using Equation 6.102 from Reference⁸³:

$$k_q = k / (\gamma * t_e) \quad [12]$$

where the thermodynamic factor (γ) is defined as:

$$\gamma = \frac{1}{2} * \left[\frac{\partial \ln(p_{O_2})}{\partial \ln(2 - \delta)} \right] \quad [13]$$

and calculated using the equilibrium δ values obtained here for air and 10 times diluted air, and t_e is the electronic transference number obtained here from literature bulk 10PCO data.⁸⁴

3. Experimental Methods

3.1 Sample Preparation

One-side polished, (100) oriented, circular, 200 μm thick, 25 mm diameter $(\text{Y}_2\text{O}_3)_{0.095}(\text{ZrO}_2)_{0.905}$ (YSZ) and magnesium oxide (MgO) single crystals (Crystec GmbH, Berlin, Germany) were used as PLD substrates. Prior to deposition, all the substrates were annealed at 1450°C for 20 hours with a 5°C/min nominal heating and cooling rate to relieve any residual internal stress. Afterwards, the 25-700°C curvature changes of the uncoated substrates were measured to ensure that any substrate residual stresses capable of producing unwanted curvature changes during later film stress-temperature measurements were adequately removed. Only substrates exhibiting 25-700°C bare wafer curvature changes less than 0.005 m^{-1} were used for subsequent Pulsed Laser PLD deposition.

Targets for PLD deposition were produced by pressing and sintering $\text{Pr}_{0.1}\text{Ce}_{0.9}\text{O}_{1.95-\delta}$ powders into dense pellets. These powders were produced using the glycine nitrate combustion method⁸⁵ using 18.2 M Ω water (Millipore, Burlington, MA), Pyrex glassware (Sigma Aldrich, St. Louis, MO), Teflon coated stir bars (Fischer Scientific, Pittsburgh, PA), a stainless steel reaction vessel (Polar Ware, Kiel, WI), 99.9% pure praseodymium nitrate (Strem Chemicals, Newburyport, MA), 99.9% pure cerium nitrate (Strem Chemicals, Newburyport, MA), and 99% pure glycine (Sigma Aldrich, St. Louis, MO) with a 1:1 glycine to nitrate ratio. After synthesis, the powder was calcined in a 99.8% pure alumina crucible (CoorsTek, Golden, CO) at 1000°C in air using 5°C/min nominal heating and cooling rates. Then, the powder was transferred to a 38 mm diameter stainless steel die (MTI Corp. Richmond, CA) and uniaxially compacted to ~63 MPa of pressure. The resulting porous pellet was then sintered at 1450°C for 20 hrs with a 3°C/min nominal heating and a 10°C/min nominal cooling rate to produce a 25 mm diameter 97% dense PLD target.

PLD was conducted with a XeF laser (Coherent, Santa Clara, CA) emitting at 353 nm. The chamber was first pumped down to 10⁻⁶ torr and then heated to a substrate temperature of ~580°C.

After the substrate temperature stabilized, the chamber was backfilled with oxygen until the pressure reached 9×10^{-3} torr. 10PCO was then simultaneously deposited onto the previously described YSZ and MgO substrates for 20 minutes using a 350 mJ laser power, a 10 Hz pulse frequency, a ~ 50 rpm sample rotation, a ~ 50 rpm target rotation, and a sample to target distance of ~ 6 cm.

After removal from the PLD, the samples had their oxygen stoichiometry re-equilibrated in air under protective 99.9% alumina crucibles at 1000°C for 1 hour with 3°C/min nominal heating and cooling rates. Given the known impact of surface impurities on the oxygen exchange properties of 10PCO,⁸⁶ the 10PCO|YSZ samples were then surface etched using standard cleanroom procedures.⁸⁷ Specifically, the samples were placed in a 65°C 50% NaOH-50% H₂O solution for 24 hours with a 100 rpm stirring speed. As shown in Figure S4 of the Supplemental Materials, this procedure was capable of removing PLD-deposited Si surface impurities without significantly altering the 10PCO surface roughness.

3.2 Film Microstructure and Crystallographic Orientation Characterization

X-Ray diffraction (XRD) was conducted using a Rigaku SmartLab diffractometer with a 44 kV voltage and a 40 mA current. Scans were carried out between 20 and 80° with a 0.01°/min scan rate and a 1 second dwell time.

Scanning electron microscopy (SEM) imaging was conducted on fractured sample cross-sections coated with ~ 5 nm of Pt using a TESCAN MIRA3 Field Emission SEM (TESCAN Inc.) using a 20 kV beam voltage.

3.3 Dual Substrate Measurements

For “Dual Substrate” measurements, the curvature of both 10PCO|YSZ and 10PCO|MgO samples were measured from 280 to 700°C with 5°C/min heating and 0.2°C/min cooling rates in 25 sccm of synthetic air (i.e. 20% O₂-80% Ar). Analysis temperatures ≥ 280 °C were chosen to avoid complications introduced by the potentially orientable elastic dipoles present in ceria below ~ 250 °C.⁶⁷ Synthetic air was chosen to avoid stress changes caused by water adsorption.⁸⁸ As shown in Figure S2 of the Supplemental Materials, multiple thermal cycles were conducted in synthetic air to ensure reproducibility, and the stress-temperature results were averaged together to produce the values reported here.

The 10PCO|MgO samples went directly from the PLD chamber to the 1000°C reoxidation furnace to the XRD to the synthetic-air-flushed Multibeam Optical Stress Sensor (MOSS) test rig in an attempt to minimize hydration of the MgO substrate. The simultaneously-produced 10PCO|YSZ samples were stored in a CaCl₂ containing desiccator for ~ 2 weeks (while the 10PCO|MgO samples were being MOSS tested) before analysis.

3.4 Chemical Strain Determinations

The $p_{O_2} = 0.21$ chemical stress data was determined by first fitting the 10PCO|YSZ stress-temperature curve with a 3rd order polynomial equation over its entire 280-700°C range. The low temperature (280-380°C) 10PCO|YSZ stress vs. temperature curve was then fitted with a linear equation. The difference between the linear extrapolation and 3rd order polynomial at high temperature was used to measure the amount of temperature-induced chemical stress. The chemical strain was then calculated from the chemical stress using the temperature dependent biaxial moduli obtained from the Dual Substrate method of Section 2.2. The 10PCO|YSZ data was chosen instead of 10PCO|MgO data for this purpose because of its lower sample noise.

Since Dual Substrate measurements were not taken in $p_{O_2} = 0.021$, the $p_{O_2} = 0.021$ chemical strain values were determined by combining the measured chemical stresses generated by switching from a p_{O_2} of 0.21 to 0.021 in the curvature relaxation measurements with the temperature dependent biaxial moduli obtained from the Dual Substrate method of Section 2.2, and adding the result to the $p_{O_2} = 0.21$ chemical strain values.

3.5 Curvature Relaxation Measurements

Prior to high temperature curvature relaxation measurements, the 10PCO|YSZ samples were heated up to 500°C in synthetic air with a 5°C/min heating rate. Curvature relaxation measurements were then conducted on 10PCO|YSZ samples from 500 to 600°C at 25°C increments, following the procedures described previously.^{40, 89-91} Wafer curvature relaxations were triggered by switching between 100 sccm of synthetic air (20% O₂-80% Ar) and 100 sccm of 10% synthetic air-90% Ar (i.e. 10 times diluted air). To minimize possible Si contamination from the fused quartz curvature relaxation test rig (which is a time-dependent process), only 1 reduction and 1 oxidation cycle were measured at each temperature between 500-575°C. Multiple oxidation/reduction cycles were then tested at 600°C to determine if the curvature measurements were reproducible with redox cycling and/or experienced gradual sample drift with time due to Si contamination.

3.6 Electrical to Chemical Oxygen Surface Exchange Conversion

Equation 12 was used to convert the Si-free literature 10PCO thin film literature k_q values from Chen et al.⁴⁵ into k values that could be compared with those measured here. This was performed using Equation 13 and the oxygen nonstoichiometry data from Chen et al.⁶¹

In an attempt to minimize sources of potential error, the R_S values from Chen et al.⁴⁵ used here for comparison were taken directly from Chen et al.⁴⁵ and were not calculated from their k_q values.

4. Results and Discussion

Figure 1 shows representative X-ray Diffraction (XRD) scans of the oxygen re-equilibrated 10PCO films (some of which are pictured in Figure S5 of the Supplemental Materials.) These results indicate that the 10PCO films were phase pure and highly-crystalline on both (100) oriented MgO and (100) oriented YSZ substrates. Further, the 10PCO films on both substrates had a similar, predominantly (100) preferred orientation. Specifically, the 10PCO on YSZ films displayed only (100) orientation, while ~97% of the 10PCO on MgO grains were (100) oriented while the rest were (111) oriented (based on the ~100:9 Figure 1a 10PCO (200):(111) intensity ratio and the 28.5:100 CeO₂ JCPDS PDF #34-394 (200):(111) intensity ratio⁹² for a randomly oriented polycrystal). This grain orientation behaviour was identical to that reported in the literature for CeO_{2-x} on (100) MgO,⁹³ CeO_{2-x} on (100) YSZ,⁹³⁻⁹⁶ and 10PCO on (100) YSZ.^{45,97} A Scherrer Equation⁹⁸ analysis indicated that the average 10PCO grain size on the MgO and YSZ substrates was ~28 nm and ~21 nm, respectively (Note, the limited number of XRD peaks resulting from the 10PCO preferred orientation prevented a more accurate Williamson-Hall⁹⁹ grain size determination. Also note that these grain sizes are lower limits because peak broadening caused by the XRD itself was not accounted for).

As indicated by the cross-sectional scanning electron microscopy (SEM) images of Figure S6 of the Supplemental Materials, the 10PCO films on MgO and YSZ were dense, laterally uniform, and 235 ± 2 nm and 230 ± 5 nm in thickness, respectively. Post analysis SEM and XRD scans (not shown) did not detect any changes in the crystallographic or microstructural character of the 10PCO films caused by the 25-700°C thermal cycling, *p*O₂ cycling, and elevated temperature holds encountered during wafer curvature testing.

Figure 2 shows representative stress-temperature curves for the 10PCO|MgO and 10PCO|YSZ samples taken with a 0.2°C/min cooling rate. As demonstrated in Figure S7 of the Supplemental Materials, 0.2°C/min was slow enough to ensure that the samples remained in thermal equilibrium as the stress-temperature data was collected. The initial increase in film stress with increasing temperature displayed by the Figure 2a 10PCO|MgO sample is consistent with the fact that from 280-500°C the 10PCO α_{tc} (which ranges from 8 to 14 ppm/K)⁶⁰ is less than the 280-500°C MgO α_t (which ranges from 13 to 14 ppm/K).⁵⁶ Similarly, the subsequent decrease in film stress with increasing temperature above ~500°C is consistent with the fact that the 500-700°C 10PCO α_{tc} (which ranges from ~14 to 24 ppm/K)⁶⁰ is greater than the 500-700°C MgO α_t (which ranges from 14 to 15),⁵⁶ due to the onset of chemical expansion in 10PCO. The constant increase in film stress with temperature for the 10PCO|YSZ sample of Figure 2b is consistent with the fact that the 280-700°C 10PCO α_{tc} (which ranges from 8 to 24 ppm/K)⁶⁰ is always larger than the 280-700°C YSZ α_t (which ranges from 9 to 10 ppm/K).⁵⁷ It is interesting to note that these thermal-expansion-mismatch induced stresses were in addition to tensile ~580°C 10PCO growth stresses of ~300

and ~250 MPa on MgO and YSZ, respectively (even larger 10PCO growth stresses have been observed in the literature⁷⁷). Note, since the critical thickness for ceria epitaxy on YSZ is <1 nm,¹⁰⁰ the film stresses here do not likely include epitaxy-induced stresses.

Figure 3 shows the temperature-dependent (100) Young's Modulus values measured here in comparison to all the 10PCO *E* measurements presently available in the literature. The slight dip in the Figure 3 *E* values is likely an artefact of the 10PCO|MgO ~400-500°C fitting error shown in Figure 2a. The ± ~10% error bars shown in Figure 3 were calculated using the procedures described in Section 2 of the Supplemental Materials and are similar in magnitude to those reported in other Dual Substrate studies.⁵⁵ The ~200 GPa constancy of the 280-700°C 10PCO *E* is similar to that observed in Ce_{0.9}Gd_{0.1}O_{1.95- δ} ¹⁰¹ and is likely the result of the small magnitude of the 10PCO δ changes encountered here.

The *E* values obtained here agreed well with the 750°C MOSS stress/XRD stain determined (100) 10PCO *E* value from Sheth *et al.*⁶³ However, they do not agree with the 600°C nano-indentation determined *E* value from Swallow *et al.*⁶² This may result from the inherent difficulty in performing reliable high temperature nano-indentation experiments or the fact that unlike all the other studies in Figure 3 (which were performed on 10PCO), Swallow *et al.*⁶² examined 20PCO. Room temperature extrapolations of the *E* values obtained here agree with the fast, but not the slow, 25°C 10PCO nano-indentation measurements in the literature.^{62, 102} This is consistent with the idea that nano-indentation-determined *E* values taken too quickly to be compromised by reorientation of the anelasticity-inducing oxygen-vacancy-generated elastic dipoles¹⁵ present in ceria below ~250°C⁶⁷ should be similar to the *E* values extrapolated from high temperature ceria samples with low, or no, amounts of orientable, oxygen-vacancy-generated elastic dipoles.

Figure 4 shows the temperature-dependent α_{tc} values measured here in comparison to all the 10PCO α_{tc} measurements presently available in the literature. Similar to the Figure 3 results which don't display a systematic difference between the *E* values obtained from bulk/micro-grained samples compared to those from thin film and/or nano-grained samples, the thin film α_{tc} values obtained here agreed very well with previous *in situ* XRD literature measurements on bulk, micro-sized grain samples.⁶⁰ The maximum ± ~8% α_{tc} error bars shown in Figure 4, calculated using the procedures described in Section 2 of the Supplemental Materials, are similar to those reported for α_t in other Dual Substrate literature studies.⁵⁵

Figure 5a and 5b show the measured 10PCO chemical strain, and the oxygen nonstoichiometry extracted from it, respectively, compared to the literature. Interestingly, the measured thin films of Figure 5a experience less in-plane chemical strain than bulk 10PCO, but experience a Figure 5b δ similar to bulk PCO. This is caused by the lower α_c values of ~0.07 for (100) oriented, thin film 10PCO^{68, 77} compared to ~0.09 for randomly-oriented bulk 10PCO.⁶⁰ The good agreement between the Figure 5b *p*O₂ = 0.21

thin film δ values obtained here and the bulk 10PCO data of Bishop *et al.*⁶⁰ may be caused in part, by the relatively low (i.e. 300 to -50 MPa) 600-700°C 10PCO film stress stresses encountered here. The δ values obtained under a p_{O_2} of 0.21 and 0.021 are also both in good agreement with other thin film 10PCO studies that did,⁶¹ and did not,⁷⁷ utilize precious metal current collectors to determine δ .

Figure 6 shows representative stress redox cycle data for a 10PCO film k tested at 600°C (redox cycle data for all tested temperatures is shown in Figure S8 of the Supplemental Materials). While a steady-state equilibrium was obtained after each p_{O_2} cycle (allowing a reliable k determination), the equilibrium film stress after each oxidation and reduction cycle was slightly altered from its previous value. This behaviour was likely not caused by Si contamination from the fused silica test rig because such a process produces a gradual stress change with time, and the equilibrium stress values after each oxygen partial pressure change are flat. This difference in equilibrium stress level with p_{O_2} cycling has been observed previously in the literature,^{77, 86} where it was attributed to stress-relaxing alterations of the grain boundary structure.⁷⁷ The fact that only one physical process is observed in the $\ln[1 - \text{normalized curvature}]$ data of Figure S9 of the Supplemental Materials suggests that whatever the mechanism, this behaviour is purely the result of, and occurs on the same timescale, as oxygen exchange into/out of the film.

Figure 7 shows the oxygen surface exchange coefficient values measured here, in comparison with other literature measurements. As seen in many other studies on various oxygen exchange materials,^{40, 103, 104} the oxidation kinetics were faster than the reduction kinetics. As postulated in other studies,^{103, 104} this is likely due to the larger δ at the beginning of the oxidation process than at the beginning of the reduction process speeding up the initial oxygen exchange. The measured k values displayed Arrhenius behaviour over the entire 500-600°C range, which is consistent with only one oxygen exchange process being active. Select tests on select samples performed with smaller p_{O_2} step sizes utilizing air and 5 times (instead of 10 times) diluted air gave K 's with similar activation energies, but with absolute values between the reduction and oxidation data, suggesting that the oxygen surface exchange kinetics remained linear at a 10 times dilution, as observed previously in the literature for other materials.¹⁰⁴

The 600°C k values measured here agreed exactly with those obtained from the optical relaxation studies of Zhao *et al.*⁸⁶ even though the samples were subjected to different thermal histories before testing (Zhao *et al.*⁸⁶ do not report re-equilibrating their samples in 1000°C air before testing, as was done here) and the specimens were grown in different Pulsed Laser Deposition chambers likely containing different impurities. The likely source of this agreement is that, as shown in Table 1 of the Supplementary Materials, the samples used for both studies were produced in the same manner, had similar final microstructures, likely had similar grain sizes and similar stress states, and did not utilize precious metal current collectors.

In contrast, the measured K 's were much lower than those determined from microbalance and EIS studies. Although Simons

*et al.*¹⁰³ attributed their observed k enhancement to grain boundary/grain orientation effects in their randomly-oriented polycrystalline films,¹⁰³ this seems unlikely to be the sole cause of the ~1000 times difference with the present results because other literature studies have only observed k differences within an order of magnitude for ceria¹⁰⁵ or lanthanum strontium cobalt iron oxide¹⁰⁶ when examining thin films with intentionally-varied crystallographic orientations. Instead, based on the documented ability of precious metals such as Pt,¹⁰⁷⁻¹⁰⁹ Ag,^{107, 110} and Au¹⁰⁸ to catalyse the oxygen exchange reaction on a variety of MIEC materials (including PCO), it seems more likely that catalytically active Pt migrated onto the surface of Simons *et al.*'s 10PCO films from the underlying Pt current collector (which was applied to the substrate before the film) during subsequent 10PCO pulsed laser deposition and/or testing. For the data from Chen *et al.* the catalytic enhancement provided by the porous Au current collectors covering 10PCO film surface may also explain the difference between EIS and κR measured k . However, additional current-collector-free tests on individual 10PCO films before and after intentionally introduced precious metal surface contamination are needed before firm conclusions can be drawn on whether precious metal surface contamination artificially enhances k .

Figure 8 shows the oxygen surface exchange resistance values measured here, compared with those from the literature. (Note that for small oxygen nonstoichiometries like those encountered here for 10PCO, the c_o in Equation 10 is not significantly affected by the oxygen nonstoichiometry and R_S can be estimated directly from k without knowledge of the oxygen nonstoichiometry, as done in the literature.^{45, 82} Even though the effect is small, all the Figure 8 10PCO R_S values were calculated using the c_o values from Figure 5b). Consistent with the behaviour observed in Figure 7, the wafer curvature measured 10PCO R_S values were significantly higher than those obtained from the precious-metal-coated EIS R_S experiments of Chen *et al.*⁴⁵ The slightly higher wafer-curvature-determined R_S activation energy, compared to that from Chen *et al.*⁴⁵ comes from the different thermodynamic factors behaviour shown in Figure 5b. The 1.6 ± 0.1 eV 10PCO wafer-curvature-determined R_S activation energy measured here is similar in magnitude to that of many other MIEC oxygen exchange materials.^{111, 112}

Figure 8 also shows that the wafer-curvature measured 10PCO R_S values were at least two orders of magnitude higher than the R_S values of the SOFC material $\text{La}_{0.6}\text{Sr}_{0.4}\text{Co}_{0.8}\text{Fe}_{0.2}\text{O}_{3-\delta}$ (LSFC). (Note, unlike EIS measurements performed on large surface area samples requiring current collectors to distribute the charge, the small lateral dimensions of the microelectrode samples used to measure the $\text{La}_{0.6}\text{Sr}_{0.4}\text{FeO}_{3-\delta}$ (LSF),¹¹¹ $\text{La}_{0.6}\text{Sr}_{0.4}\text{CoO}_{3-\delta}$ (LSC),¹¹¹ LSFC,^{111, 112} $\text{Sr}_{0.5}\text{Sm}_{0.5}\text{CoO}_{3-\delta}$ (SSC),¹¹¹ and $\text{Ba}_{0.5}\text{Sr}_{0.5}\text{Co}_{0.8}\text{Fe}_{0.2}\text{O}_{3-\delta}$ (BSCF)¹¹¹ R_S values reported in Figure 8 meant that cathode-side precious metal current collectors were not needed. Further, the trustworthiness of these microelectrode EIS R_S values is suggested by the fact that the open-circuit performance of LSF, LSFC, LSCF,

LSC, and SSC infiltrated SOFC cathodes can be successfully modelled using them^{81, 113-115}). Taken together, the data in Figure 8 suggests that low-stress, precious-metal-free, (100)-oriented 10PCO measured here performs much worse than conventional SOFC cathode materials.

Conclusions

This work demonstrates, for the first time, that a sample's mechanical response can be used to "simultaneously" measure a material's biaxial modulus, Young's Modulus, thermal expansion coefficient, thermo-chemical expansion coefficient, oxygen nonstoichiometry, chemical oxygen surface exchange coefficient (k), oxygen surface exchange resistance (R_s), strain, and stress state as function of temperature and oxygen partial pressure. Consistent with select literature measurements on bulk and thin film 10PCO, the Young's Modulus of (100)-oriented thin film 10PCO was measured to be ~ 200 GPa in air from 280-700°C. Further, the (100)-oriented 10PCO thin film thermal expansion coefficient, thermo-chemical expansion coefficient, and oxygen nonstoichiometry measured here were shown to be similar to those from other bulk and thin film 10PCO studies. The 10PCO k values measured here were also consistent with those from other current collector free techniques. Since most materials experience lattice parameter changes with changes in composition, the techniques developed here may find use for the "simultaneous" determination of the mechanical properties, thermal properties, point defect concentrations and ion-exchange properties of a variety of other materials.

Conflicts of interest

"There are no conflicts to declare".

Acknowledgements

Yuxi Ma acknowledges support from Department of Energy Award Number DE-FE0023315 and Jason Nicholas acknowledges support from the National Science Foundation CAREER Award number CBET-1254453. The microscopy work was conducted at the Michigan State Composites Center, which is supported by the NSF Major Instrumentation Program and Michigan State University. The authors would like to thank Dr. Timothy Hogan and Mr. Karl Dersch of Michigan State University for assistance with the thin film deposition. The authors would also like to thank Mr. Per Askeland for assistance with the XPS measurements.

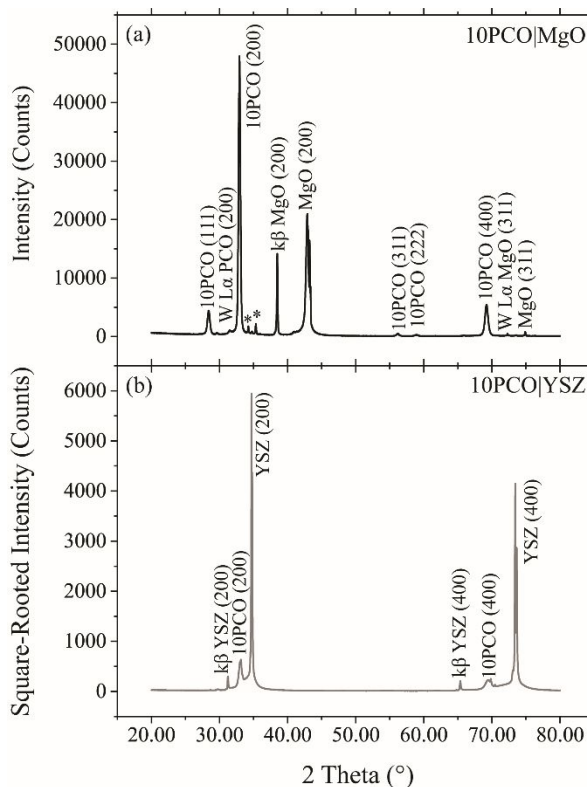


Figure 1. Representative X-Ray Diffraction (XRD) results for a) 10PCO|MgO and b) 10PCO|YSZ indexed using CeO_2 , MgO, and YSZ JCPDS card numbers 81-0792, 87-0653, and 70-4436, respectively. The asterisks denote impurity peaks not caused by the 10PCO, as proven by the bare MgO substrate XRD scans of Figure S10 in the Supplemental Materials.

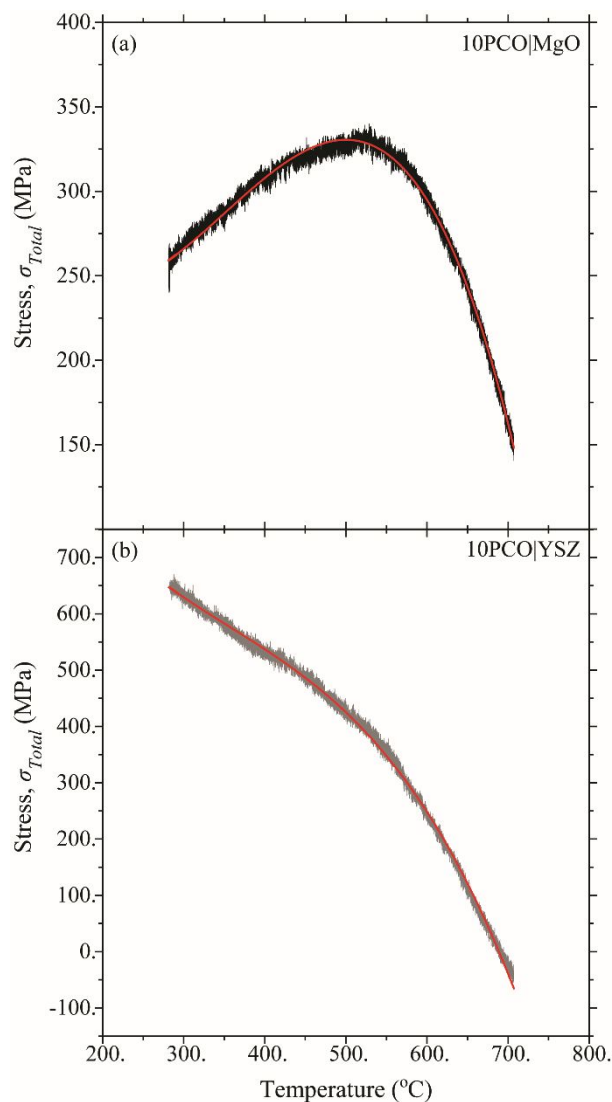


Figure 2. Representative averaged stress vs. temperature plots for a) 10PCO|MgO and b) 10PCO|YSZ. The red lines are fits to the measured data. For 10PCO|MgO $\sigma_{Total} = (486.0 \pm 1.638) + (-2.389 \pm 0.01059) * T + (0.007670 \pm 2.201 * 10^{-5}) * T^2 + (-7.020 * 10^{-6} \pm 1.479 * 10^{-8}) * T^3$ and for 10PCO|YSZ $\sigma_{Total} = (1241.7 \pm 4.065) + (-3.788 \pm 0.02622) * T + (0.008090 \pm 5.446 * 10^{-5}) * T^2 + (-7.562 * 10^{-6} \pm 3.654 * 10^{-8}) * T^3$.

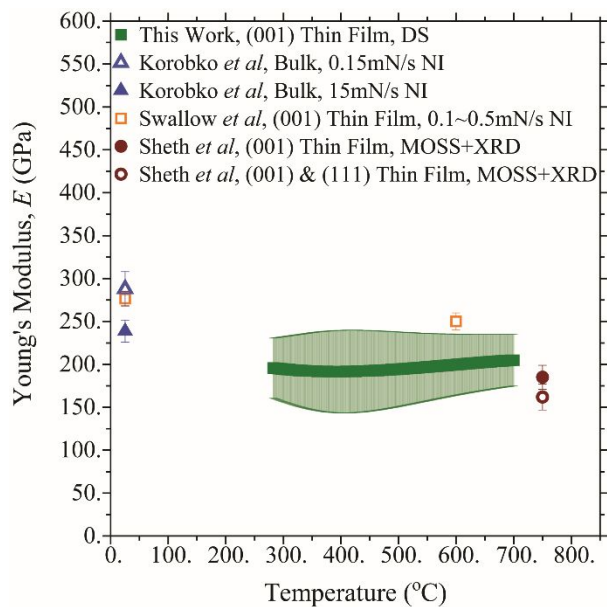


Figure 3. PCO Young's moduli values measured by the Dual Substrate method compared to the literature measurements of Korobko *et al.*,¹⁰² Swallow *et al.*,⁶² and Sheth *et al.*⁶³ (DS stands for Dual Substrate, NI stands for Nano-Indentation, MOSS stands for Multi-beam Optical Stress Sensor, and XRD stands for X-Ray Diffraction). Note, all the studies in this plot utilized 10PCO, except those by Swallow *et al.*⁶² which utilized 20PCO.

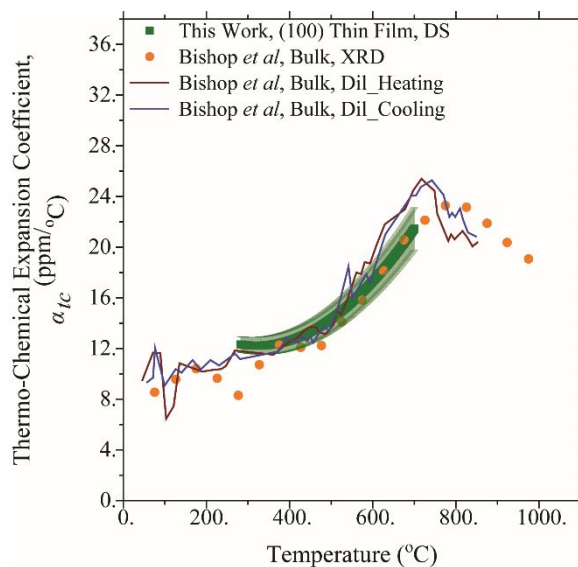


Figure 4. 10PCO thermo-chemical expansion coefficients from the Dual Substrate method compared to the literature measurements of Bishop *et al.*⁶⁰ (DS stands for Dual Substrate, XRD stands for X-Ray Diffraction, and Dil stands for Dilatometry).

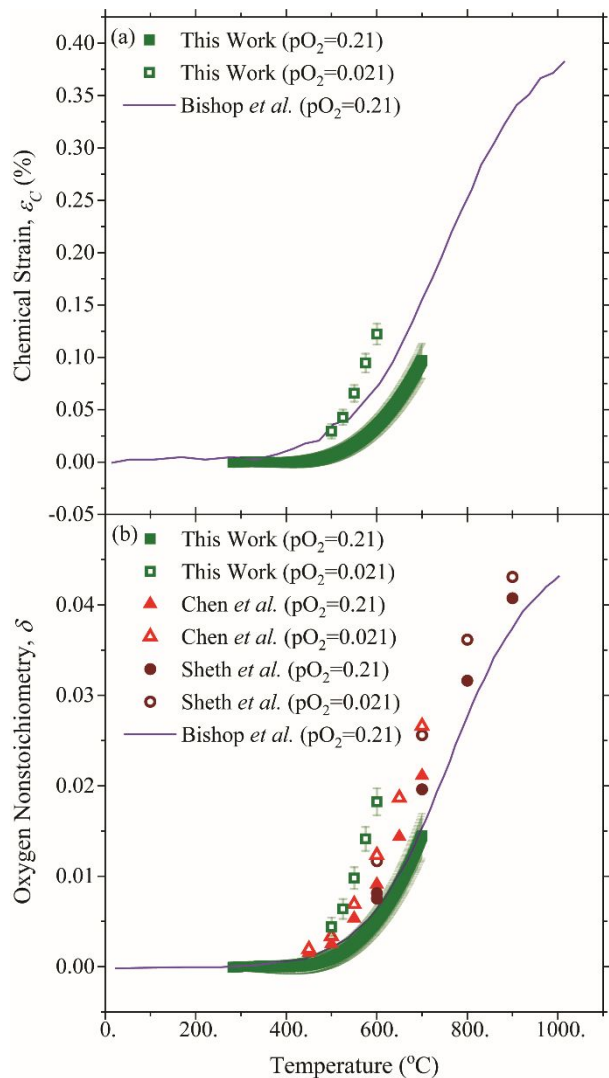


Figure 5. 10PCO (a) chemical strain and (b) oxygen nonstoichiometry values from the 10PCO|YSZ sample compared to the literature measurements of Chen *et al.*,⁶¹ Sheth *et al.*⁷⁷ and Bishop *et al.*⁶⁰

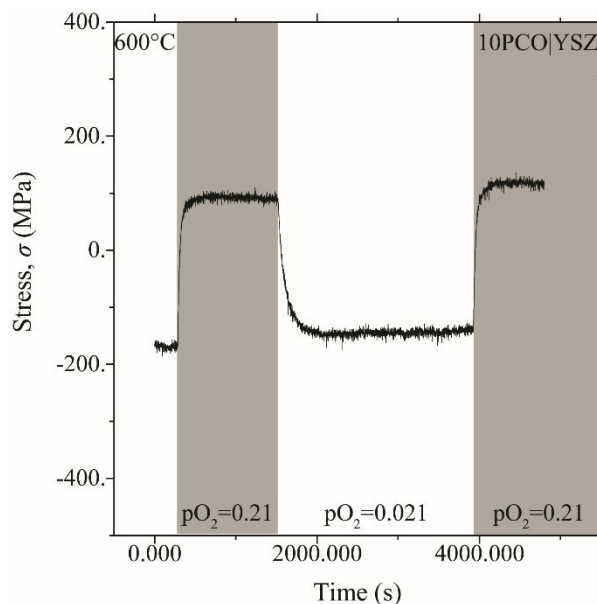


Figure 6. Representative raw curvature relaxation data for a 10PCO|YSZ sample at 600°C.

ARTICLE

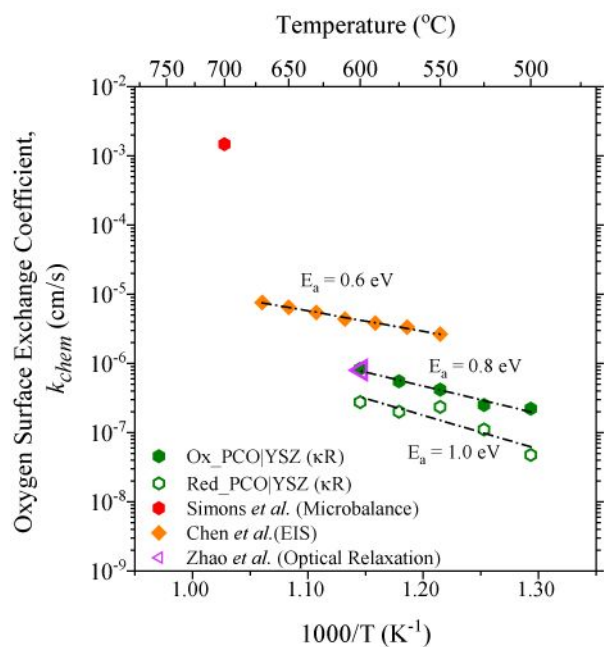
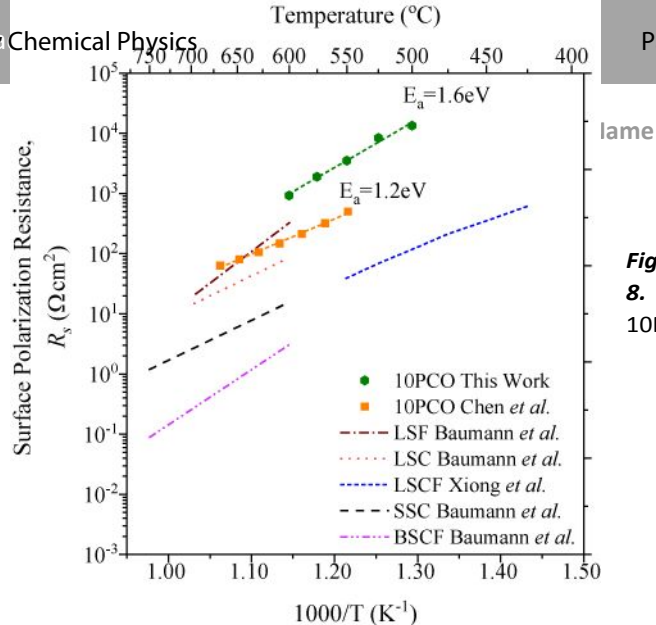


Figure 7. 10PCO chemical oxygen surface exchange coefficients from the curvature relaxation method compared to the literature measurements of Simons *et al.*¹⁰³, Chen *et al.*⁴⁵, and Zhao *et al.*⁸⁶ The curvature-determined k error is less than the size of the symbol.



lame

Figure 8.
10PCO

oxygen surface polarization resistance (R_s) values obtained here compared to the literature values for 10PCO,⁴⁵ $\text{La}_{0.6}\text{Sr}_{0.4}\text{FeO}_{3-\delta}$ (LSF),¹¹¹ $\text{La}_{0.6}\text{Sr}_{0.4}\text{CoO}_{3-\delta}$ (LSC),¹¹¹ $\text{La}_{0.6}\text{Sr}_{0.4}\text{Co}_{0.8}\text{Fe}_{0.2}\text{O}_{3-\delta}$ (LSCF)¹¹² and $\text{Sm}_{0.5}\text{Sr}_{0.5}\text{Co}_{3-\delta}$ (SSC).¹¹¹ The curvature-determined R_s error is less than the size of the symbol.

Notes and references

1. J. Maier, *Angewandte Chemie-International Edition*, 2013, **52**, 4998-5026.
2. S. Lévassieur, M. Menetrier, Y. Shao-Horn, L. Gautier, A. Audemer, G. Demazeau, A. Largeteau and C. Delmas, *Chemistry of Materials*, 2003, **15**, 348-354.
3. S. B. Adler, *Chemical Reviews*, 2004, **104**, 4791-4843.
4. A. Atkinson, S. A. Barnett, R. J. Gorte, J. T. S. Irvine, A. J. McEvoy, M. B. Mogensen, S. Singhal and J. Vohs, *Nature Materials*, 2004, **3**, 17-27.
5. Y. L. Lee, J. Kleis, J. Rossmeisl, Y. Shao-Horn and D. Morgan, *Energy Environ. Sci.*, 2011, **4**, 3966-3970.
6. T. Das, J. D. Nicholas and Y. Qi, *Journal of Materials Chemistry A*, 2017, **5**, 4493-4506.
7. K. D. Kreuer, *Chemistry of Materials*, 1996, **8**, 610-641.
8. S. D. Ebbesen, S. H. Jensen, A. Hauch and M. B. Mogensen, *Chemical Reviews*, 2014, **114**, 10697-10734.
9. G. M. Wang, H. Y. Wang, Y. C. Ling, Y. C. Tang, X. Y. Yang, R. C. Fitzmorris, C. C. Wang, J. Z. Zhang and Y. Li, *Nano Letters*, 2011, **11**, 3026-3033.
10. M. G. Walter, E. L. Warren, J. R. McKone, S. W. Boettcher, Q. X. Mi, E. A. Santori and N. S. Lewis, *Chemical Reviews*, 2010, **110**, 6446-6473.
11. W. C. Chueh, C. Falter, M. Abbott, D. Scipio, P. Furler, S. M. Haile and A. Steinfeld, *Science*, 2010, **330**, 1797-1801.
12. J. J. S. Yang, D. B. Strukov and D. R. Stewart, *Nat. Nanotechnol.*, 2013, **8**, 13-24.
13. F. Messerschmitt, M. Kubicek, S. Schweiger and J. L. M. Rupp, *Adv. Funct. Mater.*, 2014, **24**, 7448-7460.
14. R. Korobko, A. Patlolla, A. Kossoy, E. Wachtel, H. L. Tuller, A. I. Frenkel and I. Lubomirsky, *Advanced Materials*, 2012, **24**, 5857-5861.
15. T. Das, J. D. Nicholas, B. W. Sheldon and Y. Qi, *Phys. Chem. Chem. Phys.*, 2018, **20**, 15293-15299.
16. H. J. M. Bouwmeester, *Catalysis Today*, 2003, **82**, 141-150.
17. M. W. Ahn, K. S. Park, J. H. Heo, J. G. Park, D. W. Kim, K. J. Choi, J. H. Lee and S. H. Hong, *Applied Physics Letters*, 2008, **93**.
18. C. G. Granqvist, *Solar Energy Materials and Solar Cells*, 2000, **60**, 201-262.
19. A. Trovarelli, *Catalysis Reviews: Science and Engineering*, 1996, **38**, 439-509.
20. D. Marrocchelli, S. R. Bishop, H. L. Tuller and B. Yildiz, *Adv. Funct. Mater.*, 2012, **22**, 1958-1965.
21. T. Das, J. D. Nicholas and Y. Qi, *Journal of Materials Chemistry A*, 2017, **5**, 25031-25043.
22. J. D. Nicholas, Y. Qi, S. R. Bishop and P. P. Mukherjee, *Journal of the Electrochemical Society*, 2014, **161**, Y10-Y11.
23. W. H. Woodford, Y. M. Chiang and W. C. Carter, *Journal of the Electrochemical Society*, 2010, **157**, A1052-A1059.
24. A. Atkinson, *Solid State Ionics*, 1997, **95**, 249-258.
25. X. H. Liu, L. Zhong, S. Huang, S. X. Mao, T. Zhu and J. Y. Huang, *ACS Nano*, 2012, **6**, 1522-1531.
26. R. W. Hertzberg, *Deformation and Fracture Mechanics of Engineering Materials*, John Wiley & Sons, New York, 4th edn., 1996.
27. A. Kushima and B. Yildiz, *Journal of Materials Chemistry*, 2010, **20**, 4809-4819.
28. H. L. Tuller and S. R. Bishop, *Annual Review of Materials Research*, 2011, **41**, 369-398.
29. M. Kubicek, Z. H. Cai, W. Ma, B. Yildiz, H. Hutter and J. Fleig, *ACS Nano*, 2013, **7**, 3276-3286.
30. A. Fluri, D. Pergolesi, V. Roddatis, A. Wokaun and T. Lippert, *Nature Communications*, 2016, **7**.
31. R. A. De Souza, A. Ramadan and S. Horner, *Energy Environ. Sci.*, 2012, **5**, 5445-5453.
32. A. K. Sagotra and C. Cazorla, *ACS Appl. Mater. Interfaces*, 2017, **9**, 38773-38783.
33. N. Muralidharan, C. N. Brock, A. P. Cohn, D. Schauben, R. E. Carter, L. Oakes, D. G. Walker and C. L. Pint, *ACS Nano*, 2017, **11**, 6243-6251.
34. A. Karthikeyan and S. Ramanathan, *Applied Physics Letters*, 2008, **92**, 243109-243101 to 243109-243103.
35. P. Ried, P. Holtappels, A. Wichser, A. Ulrich and T. Graule, *Journal of the Electrochemical Society*, 2008, **155**, B1029-B1035.
36. P. Plonczak, M. Søgaard, A. Bieberle-Hütter, P. V. Hendriksen and L. J. Gauckler, *Journal of the Electrochemical Society*, 2012, **159**, B471-B482.
37. J. E. tenElshof, M. H. R. Lankhorst and H. J. M. Bouwmeester, *Journal of the Electrochemical Society*, 1997, **144**, 1060-1067.
38. M. Mosleh, M. Sogaard and P. V. Hendriksen, *Journal of the Electrochemical Society*, 2009, **156**, B441-B457.
39. M. Sogaard, P. Vang Hendriksen and M. Mogensen, *Journal of Solid State Chemistry*, 2007, **180**, 1489-1503.
40. Q. Yang, T. E. Burye, R. R. Lunt and J. D. Nicholas, *Solid State Ionics*, 2013, **249-250**, 123-128.
41. S. D. Park, J. M. Vohs and R. J. Gorte, *Nature*, 2000, **404**, 265-267.
42. T. S. Stefanik and H. L. Tuller, *Journal of the European Ceramic Society*, 2001, **21**, 1967-1970.
43. A. Primo, T. Marino, A. Corma, R. Molinari and H. Garcia, *Journal of the American Chemical Society*, 2011, **133**, 6930-6933.
44. M. Mogensen, N. M. Sammes and G. A. Thompsett, *Solid State Ionics*, 2000, **129**, 63-94.
45. D. Chen, S. R. Bishop and H. L. Tuller, *J Electroceram*, 2012, **28**, 62-69.
46. H. Uchida, N. Osada and M. Watanabe, *Electrochemical and Solid State Letters*, 2004, **7**, A500-A502.
47. S. R. Bishop, D. Marrocchelli, C. Chatzichristodoulou, N. Perry, M. B. Mogensen, H. Tuller and E. Wachsman, *Annual Review of Materials Research*, 2014, **44**, 205-239.
48. H. L. Tuller, S. R. Bishop, D. Chen, Y. Kuru, J. J. Kim and T. S. Stefanik, *Solid State Ionics*, 2012, **225**, 194-197.

ARTICLE

Journal Name

49. S. R. Bishop, T. S. Stefanik and H. L. Tuller, *Phys. Chem. Chem. Phys.*, 2011, **13**, 10165-10173.
50. G. G. Stoney, *Proceedings of the Royal Society of London Series A-Containing Papers of a Mathematical and Physical Character*, 1909, **82**, 172-175.
51. L. B. Freund and S. Suresh, *Thin Film Materials: Stress, Defect Formation and Surface Evolution*, Cambridge University Press, New York, NY, 2003.
52. C. A. Klein, *Journal of Applied Physics*, 2000, **88**, 5487-5489.
53. T. F. Retajczyk and A. K. Sinha, *Applied Physics Letters*, 1980, **36**, 161-163.
54. M. M. De Lima, R. G. Lacerda, J. Vilcarromero and F. C. Marques, *Journal of Applied Physics*, 1999, **86**, 4936.
55. J. Thurn and M. P. Hughey, *Journal of Applied Physics*, 2004, **95**, 7892-7897.
56. I. Suzuki, S.-i. Okajima and K. Seya, *Journal of Physics of the Earth*, 1979, **27**, 63-69.
57. H. Hayashi, T. Saitou, N. Maruyama, H. Inaba, K. Kawamura and M. Mori, *Solid State Ionics*, 2005, **176**, 613-619.
58. C. Lenser, F. Gunkel, Y. J. Sohn and N. H. Menzler, *Solid State Ionics*, 2018, **314**, 204-211.
59. R. Chiba, H. Taguchi, T. Komatsu, H. Orui, K. Nozawa and H. Arai, *Solid State Ionics*, 2011, **197**, 42-48.
60. S. R. Bishop, H. L. Tuller, Y. Kuru and B. Yildiz, *Journal of the European Ceramic Society*, 2011, **31**, 2351-2356.
61. D. Chen, S. R. Bishop and H. L. Tuller, *Chemistry of Materials*, 2014, **26**, 6622-6627.
62. J. G. Swallow, J. J. Kim, M. Kabir, J. F. Smith, H. L. Tuller, S. R. Bishop and K. J. Van Vliet, *Acta Materialia*, 2016, **105**, 16-24.
63. J. Sheth, D. Chen, H. L. Tuller, S. T. Misture, S. R. Bishop and B. W. Sheldon, *Phys. Chem. Chem. Phys.*, 2017, **19**, 12206-12220.
64. J. H. Zhao, Y. Du, M. Morgen and P. S. Ho, *Journal of Applied Physics*, 2000, **87**, 1575-1577.
65. T. Kushi, K. Sato, A. Unemoto, S. Hashimoto, K. Amezawa and T. Kawada, *Journal of Power Sources*, 2011, **196**, 7989-7993.
66. Y. Kimura, T. Kushi, S.-i. Hashimoto, K. Amezawa and T. Kawada, *Journal of the American Ceramic Society*, 2012, **95**, 2608-2613.
67. A. Kossoy, Y. Feldman, R. Korobko, E. Wachtel, I. Lubomirsky and J. Maier, *Adv. Funct. Mater.*, 2009, **19**, 634-641.
68. Y. Kuru, S. R. Bishop, J. J. Kim, B. Yildiz and H. L. Tuller, *Solid State Ionics*, 2011, **193**, 1-4.
69. P. Gao, A. Bolon, M. Taneja, Z. Xie, N. Orlovskaya and M. Radovic, *Solid State Ionics*, 2017, **300**, 1-9.
70. J. Zhang, C. Ke, H. Wu, J. Yu, J. Wang and Y. Wang, *Journal of Alloys and Compounds*, 2017, **718**, 85-91.
71. I. Suzuki, *Journal of Physics of the Earth*, 1975, **23**, 145-159.
72. X. Y. Chen, J. S. Yu and S. B. Adler, *Chemistry of Materials*, 2005, **17**, 4537-4546.
73. S. Hull, S. T. Norberg, I. Ahmed, S. G. Eriksson, D. Marrocchelli and P. A. Madden, *Journal of Solid State Chemistry*, 2009, **182**, 2815-2821.
74. S. R. Bishop, K. L. Duncan and E. D. Wachsman, *Acta Materialia*, 2009, **57**, 3596-3605.
75. S. R. Bishop, K. L. Duncan and E. D. Wachsman, *Electrochimica Acta*, 2009, **54**, 1436-1443.
76. H. W. Chiang, R. N. Blumenthal and R. A. Fournelle, *Solid State Ionics*, 1993, **66**, 85-95.
77. J. Sheth, D. Chen, J. J. Kim, W. J. Bowman, P. A. Crozier, H. L. Tuller, S. T. Misture, S. Zdzieszynski, B. W. Sheldon and S. R. Bishop, *Nanoscale*, 2016, **8**, 16499-16510.
78. D. Er, J. Li, M. Cargnello, P. Fornasiero, R. J. Gorte and V. B. Shenoy, *Journal of the Electrochemical Society*, 2014, **161**, F3060-F3064.
79. J. Crank, *The Mathematics of Diffusion*, Oxford University Press, London, 2nd edn., 1975.
80. C. W. Tanner, K.-Z. Fung and A. V. Virkar, *Journal of the Electrochemical Society*, 1997, **144**, 21-30.
81. J. D. Nicholas, L. Wang, A. V. Call and S. A. Barnett, *Phys. Chem. Chem. Phys.*, 2012, **14**, 15379-15392.
82. F. S. Baumann, J. Fleig, H.-U. Habermeier and J. Maier, *Solid State Ionics*, 2006, **177**, 1071-1081.
83. J. Maier, *Physical Chemistry of Ionic Materials: Ions and Electrons in Solids*, John Wiley & Sons, 2004.
84. S. R. Bishop, T. S. Stefanik and H. L. Tuller, *Physical Chemistry Chemical Physics*, 2011, **13**, 10165-10173.
85. L. A. Chick, L. R. Pederson, G. D. Maupin, J. L. Bates, L. E. Thomas and G. J. Exarhos, *Materials Letters*, 1990, **10**, 6-12.
86. L. Zhao, N. H. Perry, T. Daio, K. Sasaki and S. R. Bishop, *Chemistry of Materials*, 2015, **27**, 3065-3070.
87. H. Seidel, L. Csepregi, A. Heuberger and H. Baumgärtel, *Journal of the Electrochemical Society*, 1990, **137**, 3612-3626.
88. M. Shirpour, G. Gregori, R. Merkle and J. Maier, *Phys. Chem. Chem. Phys.*, 2011, **13**, 937-940.
89. J. D. Nicholas, in *Electro-Chemo-Mechanics of Solids*, eds. S. Bishop, D. Marrocchelli, N. Perry and B. Sheldon, Springer, New York, 2017, ch. 5, pp. 103-136.
90. J. D. Nicholas, *Extreme Mechanics Letters*, 2016, **9**, 405-421.
91. Q. Yang and D. J. D. Nicholas, *Journal of the Electrochemical Society*, 2014, **161**, F3025-F3031.
92. International Center for Diffraction Data Joint Committee on Powder Diffraction Standards, *Journal*, 2012.
93. N. Savvides, A. Thorley, S. Gnanarajan and A. Katsaros, *Thin Solid Films*, 2001, **388**, 177-182.
94. C.-M. Wang, S. Thevuthasan and C. H. F. Peden, *Journal of the American Ceramic Society*, 2003, **86**, 363-365.
95. D. Q. Shi, M. Ionescu, J. McKinnon and S. X. Dou, *Physica C*, 2001, **356**, 304-310.
96. N. L. Edleman, A. Wang, J. A. Belot, A. W. Metz, J. R. Babcock, A. M. Kawaoka, J. Ni, M. V. Metz, C. J. Flaschenriem, C. L. Stern, L. M. Liable-Sands, A. L. Rheingold, P. R. Markworth, R. P. H. Chang, M. P. Chudzik, C. R. Kannewurf and T. J. Marks, *Inorganic Chemistry*, 2002, **41**, 5005-5023.
97. A. Cavallaro, F. Sandiumenge, J. Gazquez, T. Puig, X. Obradors,

- J. Arbiol and H. C. Freyhardt, *Adv. Funct. Mater.*, 2006, **16**, 1363-1372.
98. A. L. Patterson, *Physical Review*, 1939, **56**, 978-982.
99. G. K. Williamson and W. H. Hall, *Acta Metallurgica*, 1953, **1**, 22-31.
100. C. Balaji Gopal, M. García-Melchor, S. C. Lee, Y. Shi, A. Shavorskiy, M. Monti, Z. Guan, R. Sinclair, H. Bluhm, A. Vojvodic and W. C. Chueh, *Nature Communications*, 2017, **8**, 15360.
101. K. Amezawa, T. Kushi, K. Sato, A. Unemoto, S.-i. Hashimoto and T. Kawada, *Solid State Ionics*, 2011, **198**, 32-38.
102. R. Korobko, S. K. Kim, S. Kim, S. R. Cohen, E. Wachtel and I. Lubomirsky, *Adv. Funct. Mater.*, 2013, **23**, 6076-6081.
103. P. Simons, H. I. Ji, T. C. Davenport and S. M. Haile, *Journal of the American Ceramic Society*, 2017, **100**, 1161-1171.
104. S. Wang, A. Verma, Y. L. Yang, A. J. Jacobson and B. Abeles, *Solid State Ionics*, 2001, **140**, 125-133.
105. M. Tsuchiya, N. A. Bojarczuk, S. Guha and S. Ramanathan, *Journal of Chemical Physics*, 2009, **130**, 174711-174711 to 174711-174719.
106. K. Develos-Bagarinao, H. Kishimoto, J. De Vero, K. Yamaji and T. Horita, *Solid State Ionics*, 2016, **288**, 6-9.
107. M. Leonhardt, R. A. De Souza, J. Claus and J. Maier, *Journal of the Electrochemical Society*, 2002, **149**, J19-J26.
108. N. H. Perry, J. J. Kim and H. L. Tuller, *Science and Technology of Advanced Materials*, 2018, **19**, 130-141.
109. H. Borchert, Y. V. Frolova, V. V. Kaichev, I. P. Prosvirin, G. M. Alikina, A. I. Lukashovich, V. I. Zaikovskii, E. M. Moroz, S. N. Trukhan, V. P. Ivanov, E. A. Paukshtis, V. I. Bukhtiyarov and V. A. Sadykov, *The Journal of Physical Chemistry B*, 2005, **109**, 5728-5738.
110. Y. H. Gong, C. Y. Qin and K. Huang, *ECS Electrochemistry Letters*, 2013, **2**, F4-F7.
111. F. S. Baumann, J. Fleig, G. Cristiani, B. Stuhlhofer, H. U. Habermeier and J. Maier, *Journal of the Electrochemical Society*, 2007, **154**, B931-B941.
112. H. Xiong, B. K. Lai, A. C. Johnson and S. Ramanathan, *Journal of Power Sources*, 2009, **193**, 589-592.
113. J. D. Nicholas and S. A. Barnett, *Journal of the Electrochemical Society*, 2010, **157**, B536-B541.
114. M. Shah, J. D. Nicholas and S. A. Barnett, *Electrochemistry Communications*, 2009, **11**, 2-5.
115. T. E. Burye, H. Tang and J. D. Nicholas, *Journal of the Electrochemical Society*, 2016, **163**, F1017-F1022.